MNRAS 000, 1–16 (2022) Preprint 27 March 2023 Compiled using MNRAS LATEX style file v3.0

# Unveiling the gravitationally unstable disc of a massive star-forming galaxy using NOEMA and MUSE⋆

Johannes Puschnig,[1,2]† Matthew Hayes,[2] Oscar Agertz,[3] Eric Emsellem,[4] John M. Cannon,[5] Jens Melinder,[2] Göran Östlin,[2] Christian Herenz,[6] Veronica Menacho[2]

[1]*Universität Bonn, Argelander-Institut für Astronomie, Auf dem Hügel 71, D-53121 Bonn, Germany*
[2]*Department of Astronomy, Oskar Klein Centre, Stockholm University, AlbaNova University Centre, SE-106 91 Stockholm, Sweden*
[3]*Lund Observatory, Department of Astronomy and Theoretical Physics, Lund University, Box 43, SE-221 00 Lund, Sweden*
[4]*European Southern Observatory, Karl-Schwarzschild-Str. 2, D-85748 Garching, Germany*
[5]*Department of Physics & Astronomy, Macalester College, 1600 Grand Avenue, Saint Paul, MN 55105, US*
[6]*European Southern Observatory, Av. Alonso de Córdova 3107, 763 0355 Vitacura, Santiago, Chile*

arXiv:2303.13858v1 [astro-ph.GA] 24 Mar 2023

2022

**ABSTRACT**

Using new high-resolution data of CO (2–1), Hα and Hβ obtained with the Northern Extended Millimeter Array (NOEMA) and the Multi-Unit Spectroscopic Explorer (MUSE) at the Very Large Telescope, we have performed a Toomre $Q$ disc stability analysis and studied star formation, gas depletion times and other environmental parameters on sub-kpc scales within the $z \sim 0$ galaxy SDSS J125013.84+073444.5 (LARS 8). The galaxy hosts a massive, clumpy disc and is a proto-typical analogue of main-sequence galaxies at $z \sim 1-2$. We show that the massive (molecular) clumps in LARS 8 are the result of an extremely gravitationally unstable gas disc, with large scale instabilities found across the whole extent of the rotating disc, with only the innermost 500 pc being stabilized by its bulgelike structure. The radial profiles further reveal that – contrary to typical disc galaxies – the molecular gas depletion time decreases from more than 1 Gyr in the center to less than ∼100 Myr in the outskirts of the disc, supporting the findings of a Toomre-unstable disc. We further identified and analysed 12 individual massive molecular clumps. They are virialized and follow the mass-size relation, indicating that on local (cloud/clump) scales the stars form with efficiencies comparable to those in Milky Way clouds. The observed high star formation rate must thus be the result of triggering of cloud/clump formation over large scales due to disc instability. Our study provides evidence that "in-situ" massive clump formation (as also observed at high redshifts) is very efficiently induced by large-scale instabilities.

**Key words:** galaxies: starburst – galaxies: star formation – galaxies: ISM – galaxies: kinematics and dynamics – techniques: interferometric – techniques: imaging spectroscopy

## 1 INTRODUCTION

Several studies based on deep field observations have revealed that at redshifts ∼3 galaxies with total (gas+stars) masses similar to the Milky Way ($\sim 10^{11}$ M$_\odot$) are already in place (Dessauges-Zavadsky et al. 2017; Elbaz et al. 2018; Tacconi et al. 2018; Cassata et al. 2020). Since the Universe was then only ∼2 Gyr old, these massive objects must have formed within a very short time, thus requiring very high star formation rates (SFRs) compared to the $z \sim 0$ Universe. In recent years, observations of galaxies at redshifts between 0 and 4 have shown that the level of star formation is mainly dictated by stellar mass and regulated by secular processes (Popesso et al. 2019). This is manifested in a tight relation between stellar mass and SFR, the so called *main sequence of star forming galaxies* (Brinchmann et al. 2004; Noeske et al. 2007; Daddi et al. 2007; Elbaz et al. 2007; Peng et al. 2010; Wuyts et al. 2011; Whitaker et al. 2012, 2014; Tomczak et al. 2016). While the slope of the relation does not vary with redshift, its intercept shifts towards higher SFRs with increasing lookback time, see for example Wuyts et al. (2011); Rodighiero et al. (2011). As shown by several studies (Tacconi et al. 2013; Genzel et al. 2015; Scoville et al. 2017; Wiklind et al. 2019), the evolution of the main sequence is driven by an increase of the (molecular) gas fraction. As a result the gas depletion time, defined as the inverse of the SFR per unit molecular gas mass, remains roughly constant even out to $z$ ∼4. The high SFRs observed on

⋆ This work is based on observations carried out under project numbers W16BS and E16AG with the IRAM NOEMA interferometer. IRAM is supported by INSU/CNRS (France), MPG (Germany), and IGN (Spain). Based on observations collected at the European Southern Observatory under ESO programme 0101.B-0703(A).
† johannes@jpuschnig.com

© 2022 The Authors

the main sequence at high-$z$ are thus mainly driven by increasing gas fractions. Although the strong evolution of the SFR with time (redshift) is relatively well constrained (Madau & Dickinson 2014), the underlying physical mechanisms that drive star formation in gas-rich discs is still a matter of debate.

Beside their large gas fractions, high-$z$ main-sequence galaxies are observed to have higher gas velocity dispersions (Förster Schreiber et al. 2009; Lehnert et al. 2009; Swinbank et al. 2012; Wisnioski et al. 2015) compared to local spirals. Additionally, their morphologies show extremely massive *clumps*, exhibiting considerable fractions of the total mass. Initially, this was interpreted in the context of "bottom up" structure formation as an ongoing process of merging. However, with the advent of near-infrared integral field spectroscopy, in some of the clumpy galaxies, disc structures were found that are characterized by significant rotation (Genzel et al. 2006, 2008), a sign for associated structures rather than mergers. However, some fraction of them may still be ongoing mergers (Weiner et al. 2006; Förster Schreiber et al. 2009; Puech 2010; Rodrigues et al. 2017). The observed discs host giant clumps with masses of $M_{\rm cl} \lesssim 10^9\,{\rm M}_\odot$. It has been proposed that such clumps result from the fragmentation of massive gas discs driven by gravitational instability (Agertz et al. 2009b; Dekel et al. 2009; Bournaud et al. 2012; Romeo & Agertz 2014). Thus, the mode of star formation in gas-rich systems seems fundamentally different compared to the star formation within spiral arms as found in most galaxies at $z \sim 0$.

Much numerical work has been undertaken in the last few years to study gravitational fragmentation scenarios. But in early simulations, inefficient thermal feedback of supernovae resulted in overcooling, which then enhanced disc instability and star formation and led to an overproduction of giant clumps (Ceverino & Klypin 2009; Agertz et al. 2009b). More recently, various works within cosmological simulations and simulations of isolated disc galaxies were again focusing on disc fragmentation at high-$z$, but including novel feedback recipes which systematically led to less fragmentation even in massive gas-rich discs and generally lower clump masses in the range $10^7$–$10^8\,{\rm M}_\odot$ (Tamburello et al. 2015; Behrendt et al. 2015; Moody et al. 2014; Mandelker et al. 2017; Oklopčić et al. 2017). It was further proposed that some of the most massive observed star forming clumps might not be the result of "in-situ" disc fragmentation, but rather they could be accreted cores of massive satellite galaxies (Mandelker et al. 2017; Oklopčić et al. 2017). Thus, to date the question of whether massive clumps are a result of "in-situ" disc fragmentation or the product of accreted cores of massive satellite galaxies remains unanswered and needs iterations on both ends, theory and observations. The observational difficulty is that at high-$z$ the spatial resolution is often too coarse to constrain relevant physical parameters (turbulence, density, timescales related to star formation). Only gravitational lensing may help to reveal details about the clumpy discs at $z \sim 1-3$ (Dessauges-Zavadsky et al. 2019).

Despite the difficulties, recent observations support galaxy-wide disc instabilities as a cause of the clumpy nature, e.g. Dessauges-Zavadsky & Adamo (2018) showed that the clump mass function at $z$ ~1–3 follows a power-law consistent with turbulence being the driving mechanism. Moreover, the DYNAMO survey (Fisher et al. 2014), targeting extremely rare *local* clumpy gas-rich disc galaxies as a proxy for high-$z$ galaxies, revealed clump properties that favour clump formation induced by galaxy-wide disc instabilities (Fisher et al. 2017; White et al. 2017; Fisher et al. 2019).

In this paper, we present new highly-resolved NOEMA CO (2–1) and MUSE Hα observations of LARS 8, a clumpy $z \sim 0$ galaxy drawn from the *Lyman Alpha Reference Sample* (Östlin et al. 2014; Hayes et al. 2014). Given the basic properties of the galaxy (see Table 1) with a stellar mass of ~$10^{11}$ $M_\odot$ and a SFR of ~30 $M_\odot$ yr$^{-1}$, LARS 8 resembles main-sequence galaxies at high-$z$. The LARS galaxy is also known to be rotationally supported (Herenz et al. 2016; Puschnig et al. 2020), just like face-on disc galaxies typically observed at high-$z$ (compare Figure 1). Herenz et al. (2016) and Micheva et al. (2018) further revealed the existence of shells at large galactocentric radii, caused by a merger event that LARS 8 must have undergone recently. Using deep high-resolution 21 cm observations, Le Reste et al. (2022) found a large neutral gas reservoir westwards of the optical galaxy disk. The galaxy is known to have a relatively high gas fraction of 27 percent, a gas depletion time of ~1.2 Gyr (Puschnig et al. 2020) and a clumpy morphology. These properties make LARS 8 an ideal laboratory to study clump formation in a gas-rich disc galaxy.

**Table 1.** Properties of LARS 8 (see Tables 1, 9 and 10 of Puschnig et al. 2020). † The metallicity $Z$ was derived by Östlin et al. (2014) using the $R_{23}$-$P$ relation and is given in units of $12+\log({\rm O/H})$. ‡ The blue-band diameter of the 25 mag arcsec$^{-2}$ isophote was derived from SDSS g-band observations using an SQL query on SDSS DR7. Since the SDSS g-band isophote is typically ~1.3 times larger than those measured in the Johnson B band, the g-band diameter was divided by that factor.

| $D_{\rm L}$ | log $M_*$ | $Z^\dagger$ | SFR | $D_{25}^\ddagger$ | $f_{\rm gas}$ |
|---|---|---|---|---|---|
| [Mpc] | [$M_\odot$] | | [$M_\odot$ yr$^{-1}$] | ["] | [%] |
| 167.5±12 | 10.97±0.10 | 8.51 | 30±8 | 30.8 | 27±16 |

The paper is organised as follows. In Section 2 we inform about the spectroscopic observations our results are based on. The methods and tools we use to convert the observables into physical parameters (e.g. star formation rates, mass surface densities, dynamical parameters) are outlined in Section 3. The results are presented in Section 4 and subsequently discussed and compared to related works in 5. Section 6 concludes the paper with a summary.

Throughout the paper, we adopt a cosmology with $H_0$=70, $\Omega_{\rm M}$=0.3 and $\Omega_{\rm vac}$=0.7.

## 2 OBSERVATIONS AND DATA REDUCTION

### 2.1 NOEMA CO (2–1) cube

We observed LARS 8 in a single pointing under programs W16BS and E16AG with the IRAM Northern Extended Millimeter Array (NOEMA) using eight antennas in configurations A and D, providing maximum baselines of ~760 m and ~180 m respectively. The target line, CO (2–1), was observed with the WideX correlator (bandwidth ~3.6 GHz) using a tuning frequency of 222.044 GHz, corresponding to the systemic velocity derived from H I observations (Pardy et al. 2014). We further performed *on-the-fly* mapping of LARS 8 with the IRAM 30m telescope under programs 064-15 and 178-15, allowing us to include short spacing visibility data.

Extended array observations were executed on December 15, 2016 for a total on-source time of 5.2 hours under good weather conditions with a precipitable water vapour (PWV) of ~1.8 mm. Compact array observations were executed on three days during May 2017 for a total on-source time of 6.3 hours under average weather conditions with a PWV of ~2–3 mm.

The absolute flux scale of the configuration A data was calibrated on LKHA101 using a model flux of 0.54 Jy. The sources

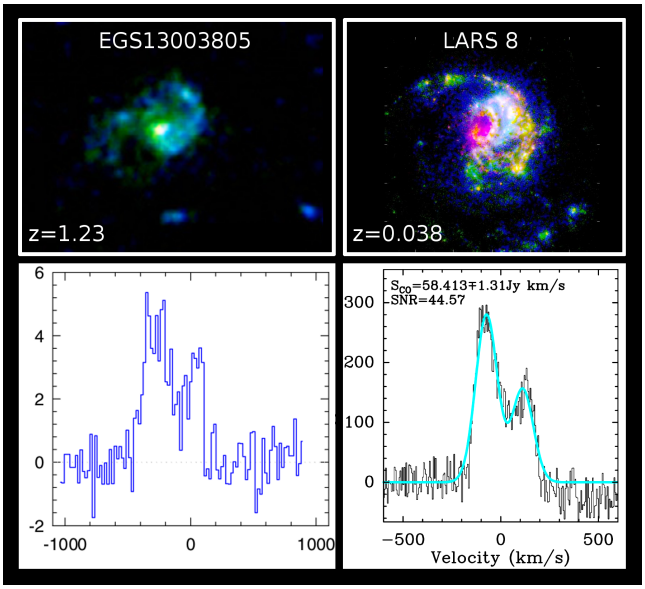



**Figure 1.** High-$z$ target from the PHIBBS survey (Tacconi et al. 2013) versus LARS 8 (Puschnig et al. 2020). The optical morphologies (*top panel*) as well as the CO line emission (*bottom panel*) are remarkably similar.

1222+216 and 3C273 were used as phase and amplitude calibrators. Average polarization mode was chosen for the amplitude calibration, because the signal was found to be polarized. 3C84 was used as bandpass calibrator.

The absolute flux scale of the configuration D data obtained on May 8, 2017 was calibrated on MWC349 with a model flux of 1.87 Jy. For the observations executed on May 2 and May 3, MWC349 data was not available and 3C273 was used instead, assuming a model flux of 7.65 Jy, as measured on May 8. 1236+077 and 3C273 were used for phase and amplitude calibration, whereas 3C273 was also used as bandpass calibrator.

All observations were calibrated using the IRAM reduction pipeline `GILDAS/CLIC`[1]. Data flagging was performed manually taking into account tracking errors, pointing and focus offsets as well as quality assessment through outlier rejection in time versus amplitude and phase plots as well as large phase discrepancies between the two polarizations. We remark that for the configuration A observations, for one of the antennas tracking errors of more than 4" were reported. All baselines including this antenna were thus rejected.

Merging of the calibrated visibilities and short spacing correction were performed in the `GILDAS/mapping` environment, which was also used for imaging. Robust weighting of 0.5 was found to lead to a good compromise between sidelobe suppression and spatial resolution, both of which are important for our science case. Cleaning was done using the Högbom algorithm (Högbom 1974) and a central circular support of 6" diameter. The final clean cube has an r.m.s. noise of 0.8 mJy/beam at a velocity resolution of 10 km/s. The synthetic beam size is 0.61"x0.37" with a position angle of 36°.

As LARS 8 is substantially extended compared to NOEMA's ~23" field of view at the observed frequency, a primary beam correction was finally performed using the `PRIMARY` task within the `GILDAS/mapping` environment.

[1] `http://www.iram.fr/IRAMFR/GILDAS/`

### 2.2 MUSE observations and data reduction

We observed LARS 8 with the Multi-Unit Spectroscopic Explorer (MUSE; Bacon et al. 2010) integral field spectrograph, mounted at Unit Telescope 4 of the Very Large Telescope (VLT). Spectra were obtained on the night of 18 May 2018 under conditions of new moon, airmass lower than 1.2, and with a V-band seeing of 0.″8. We obtained four observations of the main target, each rotated by 90 degrees compared to the previous to minimize fixed pattern noise from the image slicers, using integration times of 650 seconds. Because LARS 8 occupies a major fraction of the MUSE field-of-view, we also obtained a separate sky frame from an adjacent empty pointing using an integration time of 120 seconds. Data were reduced using Version 2.6 of the ESO pipeline, using standard methods and paying special attention to the removal of low surface brightness emission in strong nebular lines.

## 3 METHODS

Here we briefly describe the routines and tools that we used to obtain physical parameters from the observations. In subsections 3.1–3.3 we explain how the observed data cubes are prepared for further scientific analysis, i.e. the convolution to a common resolution and the derivation of moment maps.

Subsections 3.4–3.6 summarize the assumptions and constraints used to convert the observables into physical quantities such as star formation rates, stellar and gas surface densities.

In 3.7 and 3.8 the routines for the characterisation of the dynamics of the galaxy's gaseous and stellar components are presented. These dynamical quantities finally allow to constrain the gravitational instability via the Toomre parameter (see Section 3.9).

We conclude in 3.11 and 3.12 with a brief description of how individual molecular gas clouds are identified in the NOEMA cube and how we use previously derived physical quantities to estimate the dynamic equilibrium pressure.

### 3.1 Convolution of the NOEMA data cube to a common resolution

Given the slightly lower spatial resolution of the optical data cube compared to our radio data, we convolve the latter to match the resolution of the MUSE observations. To do so, we first deconvolve the elliptical NOEMA beam from the circularized target beam (based on MUSE cube). The resulting convolution kernel is then applied onto the 3D NOEMA cube (plane-by-plane) using the `scipy.signal.convolve` package (Virtanen et al. 2020). The circularized synthetic beam size of the matched-resolution NOEMA CO (2–1) data cube is 0.78". Note that throughout the paper we make use of the native resolution CO (2–1) data whenever possible (clump identification, Toomre disc stability analysis). Only plots that include both star formation rates (from Hα) and properties derived from the CO observations are based on the matched-resolution data.

### 3.2 MUSE line extraction of H$\alpha$, H$\beta$ and continuum subtraction

From the reduced MUSE cube, we first extract a fixed spectral range around the observed Hα and Hβ lines, using $z$=0.0382531 as the redshift and an extraction window of ±420 km/s, centered on the systemic line-center (corresponding to $z$). We ensured that the [N II]

lines are outside the extracted line window of Hα. In order to define the continuum level at each line, individual spectral windows were defined blueward and redward of each emission line, after manual inspection of the spectral cube. For Hα, suitable windows were found between -2500 and -1500 km/s and from 3000 to 4000 km/s. Hβ continuum levels were evaluated between -4000 and -2000 km/s as well as within the range of 2000 and 4000 km/s. The continuum correction for each line was then performed via subtraction of a linear fit, obtained from regression (using the python `lmfit` package) of the flux within the given velocity intervals.

### 3.3 Moment maps of CO (2–1) and optical emission lines

We generate moment zero maps of CO (2–1), Hα and Hβ via summation of the flux in masked channels, using the approach of "dilated masking". In the NOEMA cube, peak channels were identified that have a more than 4-sigma strong signal in at least three adjacent channels. The mask was then expanded in velocity space as long as the flux in two adjacent channels was above a 2-sigma limit. Additionally, we only allow connected spatial regions that cover at least the size of the synthetic beam of our observations. Moment maps of Hα and Hβ were created in a very similar manner, i.e. we identified channels with 4-sigma peaks and subsequently grow the mask down to a level of 2-sigma. However, given the lower spectral resolution of the MUSE data cubes, we allow to mask even single channels in velocity space rather than a number of adjacent ones.

First and second moment maps were created using the same masks, with moment one being the intensity-weighted mean velocity found under the masked channels and moment two being the intensity-weighted r.m.s. velocity scatter. Moment maps are shown in Figures 2.

The uncertainties of our moment maps are calculated via Gaussian error propagation using the r.m.s. outside the line masks as an estimate for the uncertainty of each masked channel.

### 3.4 Star formation rates from MUSE H$\alpha$

In order to obtain the intrinsic, extinction-corrected Hα flux, we calculate the dust attenuation from the Balmer decrement using the Cardelli et al. (1989) attenuation law and assume case B recombination at $10^4$ K and an intrinsic, theoretical Hα/Hβ ratio of 2.86. The average extinction E(B-V) within an aperture of 5 arcsec radius enclosing the center of the galaxy – and thus covering the main part of the NOEMA field-of-view – is 0.7 mag with a maximum value of 1.2 mag in the central pixel and values as low as 0.2 mag in the outer region.

We first convert the extinction-corrected Hα flux from erg/s/cm$^2$ into the corresponding luminosity ($L_{\mathrm{H}\alpha}$) in erg/s using a luminosity-distance of 167.5 Mpc. The star formation rates (SFRs) in units of $\mathrm{M}_\odot\ \mathrm{yr}^{-1}$ per pixel are then calculated using the calibration of Calzetti et al. (2012): $\mathrm{SFR}=5.5\ 10^{-42}\ L_{\mathrm{H}\alpha}$. These SFRs are then converted into surface densities in units of $\mathrm{M}_\odot\ \mathrm{yr}^{-1}\ \mathrm{kpc}^{-2}$ ($\Sigma_{\mathrm{SFR}}$) taking into account the cosine correction factor (cos $i$) for the galaxy inclination $i$ of 50° that we found from the rotation curve (see Section 3.7).

### 3.5 Stellar surface density

A stellar mass map of the galaxy is constructed by performing a pixel spectral energy distribution fit using the HST FUV and optical broad band data from the LARS project. The fitting code "the Lyα eXtraction Software" (Östlin et al. 2014, Melinder et al. in preparation) uses two single stellar populations with four free parameters: stellar mass for the two components, stellar age, and stellar extinction (only one of the populations have a varying age and extinction, the other one is kept at an age of 10 Gyrs and an E(B-V)$_s$ of 0). The fit is performed for each pixel (or spatial bin) to produce maps of stellar continuum fluxes, mass, age, and extinction. The uncertainties on the stellar masses are estimated within the code using Monte Carlo simulations, in which random noise (corresponding to the r.m.s. in each pixel after drizzling) is added to the originally measured value. The final uncertainty is then the standard deviation obtained from the measurements in all Monte Carlo simulations. For details on the code and the data used for LARS 8 we refer the reader to Östlin et al. (2014). To find the stellar surface density radial profile we co-add the stellar mass maps of the two components and measure the mean mass surface density in elliptical annuli that exactly match those used for the NOEMA and MUSE data. Finally, the derived mean surface densities ($\Sigma_*$) were corrected for inclination using the same quantities as for $\Sigma_{\mathrm{SFR}}$. The scale length of the stellar disc, $l_*$, was derived from the stellar mass map by fitting an exponential function to the inclination corrected mass profile.

### 3.6 Molecular gas surface density, depletion time and gas fraction

We convert our measured CO (2–1) fluxes $S_{\mathrm{CO}}$ (in units of Jy km s$^{-1}$ beam$^{-1}$) to CO luminosities using the definition of $L'_{\mathrm{CO}}$ by Solomon & Vanden Bout (2005):

$$L'_{\mathrm{CO(2-1)}} = 3.25\ 10^7\ S_{\mathrm{CO(2-1)}}\ \nu_{\mathrm{obs}}^{-2}\ D_{\mathrm{L}}^2\ (1+z)^{-3} \quad (1)$$

$L'_{\mathrm{CO(2-1)}}$ is then given in K km s$^{-1}$ pc$^2$, $z$ is the redshift, $D_{\mathrm{L}}$ the luminosity distance in Mpc and $\nu_{\mathrm{obs}}$ the observed frequency in GHz. For the conversion from $L'_{\mathrm{CO(2-1)}}$ to molecular gas masses we first need to down-convert to the luminosity of the J=1–0 line ($L'_{\mathrm{CO(1-0)}}$), for which we assume a line ratio CO(2–1)/(1–0) of 0.7, which is typically observed in several types of galaxies (Saintonge et al. 2017; den Brok et al. 2021). Subsequent multiplication with the conversion factor $\alpha_{\mathrm{CO}}$ finally leads to the molecular gas masses ($M_{\mathrm{H_2}}$). Here we use $\alpha_{\mathrm{CO}} = 4.5$ that we derived previously using a metallicity-dependent approach (Puschnig et al. 2020). This value is similar to $\alpha_{\mathrm{CO}}$ in the Milky Way (Bolatto et al. 2013). We stress that our choice of $\alpha_{\mathrm{CO}}$ is based on a galaxy-wide average. A lower conversion factor might be applicable in the center of the galaxy due to lower CO optical depths driven by a large velocity dispersion. However, to date, no data (e.g. $^{13}$CO) is available to assess any radial trend of the conversion factor in LARS 8. Again, the final gas mass surface density map ($\Sigma_{\mathrm{H_2}}$) was corrected for the inclination of the galaxy. The molecular gas depletion time $\tau_{\mathrm{depl}}$ and the gas fraction $f_{\mathrm{gas}}$ were calculated in the following way:

$$\tau_{\mathrm{depl}} = \frac{M_{\mathrm{H_2}}}{SFR} \quad (2)$$

$$f_{\mathrm{gas}} = \frac{M_{\mathrm{H_2}}}{M_{\mathrm{H_2}} + M_*} \quad (3)$$

### 3.7 Molecular gas rotation curve analysis

We use $^{3D}$`BAROLO` (Di Teodoro & Fraternali 2015) to derive the galaxy rotation curve from the NOEMA CO (2–1) data cube. The software iteratively fits 3D tilted-ring models to the cube and solves

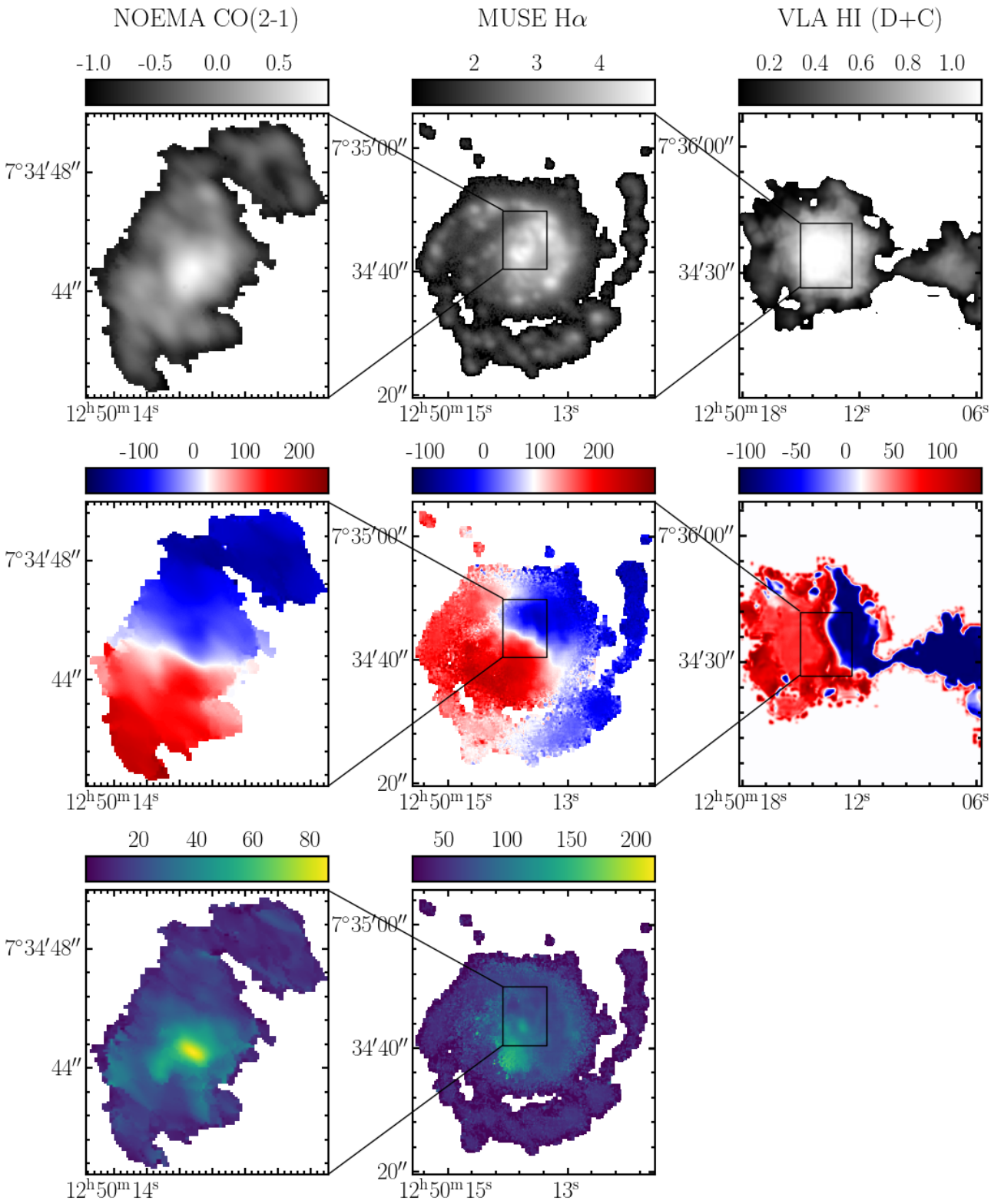



**Figure 2.** Maps derived from NOEMA CO (*left column*), MUSE Hα (*middle column*) and VLA HI 21cm (*right column*; Le Reste et al. 2022) data cubes. The top row moment-0 maps are given in units of Jy km s$^{-1}$ beam$^{-1}$ on a logarithmic scale for CO, $10^{-20}$ erg s$^{-1}$ cm$^{-2}$ on a logarithmic scale for Hα and $10^{21}$ cm$^{-2}$ on a linear scale for HI. The moment-1 and moment-2 maps in the middle and bottom rows are given in km s$^{-1}$.

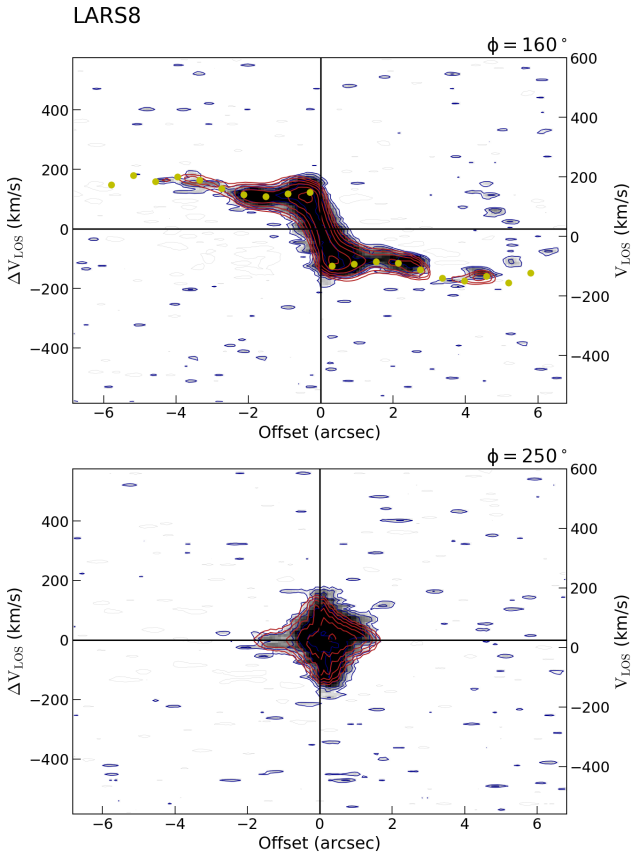



**Figure 3.** NOEMA CO (2–1) position-velocity diagram along the major axis (*top panel*) and minor axis (*bottom panel*) of LARS 8. The yellow-brown points indicate the radial bins of the derived rotation curve.

in each ring for inclination, position angle (PA), rotation velocity and velocity dispersion. We ran the software several times to experiment with input parameters such as pixel coordinates of the kinematic center, fixating systemic velocity, inclination and/or PA. Despite the fact that the algorithm robustly constrained inclination and PA we ultimately decided to fix the two parameters (for each ring) to 50 and 160 degrees respectively, while leaving the position of the kinematic center as free parameter. The free parameters derived for each 0.61" wide ring (i.e. the major axis of the beam) are thus the rotation velocity, the velocity dispersion ($\sigma_g$) and the coordinates of the kinematic center. A summary of the results is shown in Table 2. The position-velocity diagram and the smoothed and interpolated rotation curve obtained using these constraints are shown in Figures 3 and 4. A comparison between observed and modeled quantities is found in Appendix A1.

### 3.8 Stellar velocity dispersion

We use the Penalized Pixel-Fitting method (pPXF) developed by Cappellari & Emsellem (2004); Cappellari (2017) to measure stellar velocity dispersion ($\sigma_*$). We used a python wrapper developed in the course of the PHANGS-MUSE survey by F. Belfiore and I. Pessa (Belfiore et al. 2022; Emsellem et al. 2022) and based on the gist package (Galaxy IFU Spectroscopy Tool; Bittner et al. 2019). As required by pPXF, we first resample the MUSE data to a logarithmic wavelength axis using a channel size of 50 km s$^{-1}$. Following

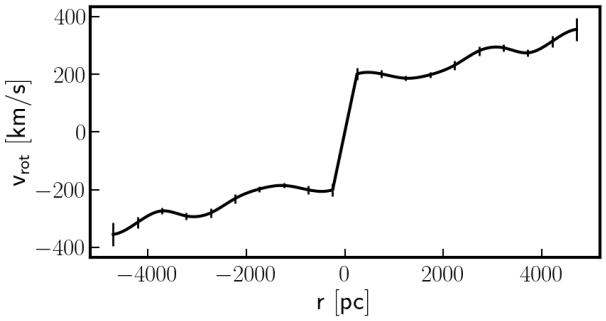



**Figure 4.** Smoothed and interpolated rotation curve (before inclination correction) derived for LARS 8 from the NOEMA CO (2–1) cube.

**Table 2.** Kinematic properties for elliptical rings.

| Radius ["] | $v_{rot}$ [km/s] | $\sigma_g$ [km/s] | i [°] | PA [°] |
|---|---|---|---|---|
| 0.305 | 154±17 | 11±4 | 50 | 160 |
| 0.915 | 154±11 | 28±7 | 50 | 160 |
| 1.525 | 142±7 | 20±4 | 50 | 160 |
| 2.135 | 151±7 | 17±4 | 50 | 160 |
| 2.745 | 176±12 | 17±6 | 50 | 160 |
| 3.355 | 215±12 | 11±7 | 50 | 160 |
| 3.965 | 223±10 | 9±5 | 50 | 160 |
| 4.575 | 210±9 | 6±5 | 50 | 160 |
| 5.185 | 240±15 | 8±4 | 50 | 160 |
| 5.795 | 272±30 | 7±4 | 50 | 160 |

Emsellem et al. (2022), this channel size is sufficient to Nyquist sample the line spread function of MUSE for wavelengths at approximately 7000 Å, while over-sampling it at the blue end. In order to avoid strong sky residuals the wavelength range for fitting was limited to 4850–7000 Å. In the following we briefly describe the fitting routine as implemented in pPXF. For the stellar continuum fitting the E-MILES simple stellar population models of Vazdekis et al. (2016) are used in combination with a Chabrier (2003) initial mass function, BaSTI isochrones (Pietrinferni et al. 2004), eight ages (0.15–14 Gyr), and four metallicities ([Z/H] = [-1.5, -0.35, 0.06, 0.4]). Thus, a total number of 32 templates are used. Spectral ranges of strong ionised gas emission lines are masked using a width of ±400 km s$^{-1}$. Since E-MILES offers a higher resolution than our MUSE data, the templates are convolved to the spectral resolution of our data, using an appropriate wavelength-dependent kernel. We fitted four moments of the line-of-sight velocity distribution: velocity, velocity dispersion, h3 and h4. To derive the stellar kinematics we make use of additive Legendre polynomials (12th order, in the spectral direction), and no multiplicative polynomials. The uncertainties on the kinematic parameters are formal errors as given by pPXF.

In the literature, the stellar velocity dispersion in galaxies is often estimated from the stellar surface density following the prescription of Leroy et al. (2008):

$$\sigma_* = 1.67 \sqrt{\frac{2\,\pi\,G\,l_*}{7.3}}\,\Sigma_*^{0.5}, \quad (4)$$

with $\Sigma_*$ being the observed stellar surface density in SI units (kg m$^{-2}$), and $l_*$ being the stellar scale length (=630 pc measured via fitting of an exponential profile to the data) in $m$. The underly-

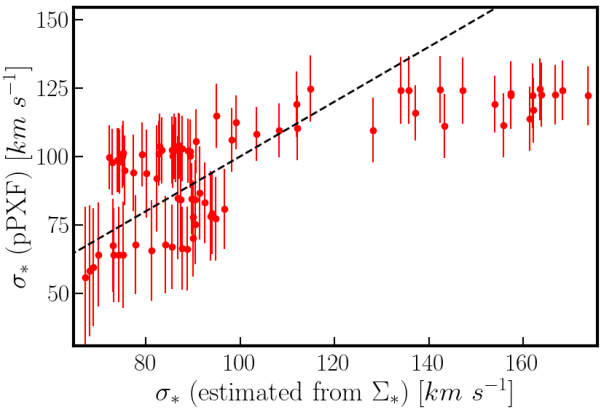



**Figure 5.** Comparison of radial averages of the velocity dispersion derived from MUSE (*y-axis*) and estimated using the prescription of Leroy et al. (*x-axis*). The vertical errorbars show the propagated uncertainties of the measurements in each radial ring.

ing assumptions of the equation are the following: the exponential stellar scale height $h_*$ of the galaxy does not vary with radius, and $h_*$ is related to the stellar scale length $l_*$ via $l_*/h_*$=7.3±2.2, i.e. the flattening ratio measured by Kregel et al. (2002). It is further assumed that the disc is isothermal in the z-direction and hydrostatic equilibrium then allows one to derive $\sigma_*$ from the observed stellar surface density $\Sigma_*$ and the estimated stellar scale height. Finally a fixed ratio of 0.6 between the radial and vertical component of the velocity dispersion is assumed, which is reasonable for most late-type galaxies (Shapiro et al. 2003). We refer the reader to the appendix of Leroy et al. (2008) for more details.

A comparison of radial averages of the velocity dispersion derived from MUSE and estimated as explained above is shown in Figure 5. We find for LARS 8 that in particular in the central region where the velocity dispersion is highest, the estimates overshoot the true (MUSE-based) values by up to approximately 40 percent.

### 3.9 Toomre $Q$ disc stability

As gravitational instability is believed to hold a key part in driving gas turbulence (Agertz et al. 2009a; Krumholz & Burkhart 2016), we consider a theoretical framework to evaluate this instability. One of the most common ways of quantifying this instability is Toomre's $Q$ parameter (Toomre 1964), which governs the stability of a smaller patch inside a disc system. The Toomre parameter for an axisymmetric, fluid disc with a differential rotation, can be determined by analysing the response of the disc to a small perturbation. The growth of this perturbation is driven by gravity, expressed as a surface density wave function. By evaluating the dispersion relation, first shown by Safronov (1960), Toomre (1964) found the condition:

$$Q_g = \frac{\kappa\,\sigma_g}{\pi\,G\,\Sigma_g} > 1 \tag{5}$$

for the disc being locally stable against graviational collapse. In this work we compute the epicyclic frequency $\kappa$ as $1.41\ \frac{v(r_{\rm gal})}{r_{\rm gal}}\ \sqrt{1+\beta}$ and $\beta = \frac{d\log\ v(r_{\rm gal})}{d\log\ (r_{\rm gal})}$. For $Q_g$<1, the disc is locally unstable. In this equation, $\kappa$ is the epicyclic frequency, $\Sigma_g$ is the gas surface density, $\sigma_g$ is the gas velocity dispersion (from the rotation curve analysis) and $G$ is the gravitational constant. The physical meaning of $\kappa$ can be thought of as the rotational support against collapse, $\sigma$ is the pressure support against collapse and $\Sigma$ sets the level of self-gravity driving the instability. An implementation of the method to compute $Q_g$ is provided via GitHub by Puschnig (2020)[2], including a working example. The above method can be expanded to a disc filled with star particles and differ only slightly from the approach of a fluid:

$$Q_* = \frac{\kappa\,\sigma_*}{3.36\,G\,\Sigma_*} \tag{6}$$

Combining the Toomre parameters for stars and gas is a necessary step to determine the stability of a multi-component disc, which is the case for most galaxies. We assume that $\kappa$ is the same for both the gaseous and the stellar disc, i.e. that gas and stars follow the same rotation. We stress that the combined $Q$ is derived such that it also obeys the instability criterion of $Q$ ~1. There have been several different approaches to combining $Q$ parameters and an extensive look into different methods was done by Romeo & Falstad (2013). In this paper, we use the approximation of Romeo & Falstad (2013):

For $Q_* > Q_g$ (gas dominated regime):

$$\frac{1}{Q} = \frac{1}{Q_g} + \frac{CF}{Q_*} \tag{7}$$

For $Q_* <= Q_g$ (star dominated regime):

$$\frac{1}{Q} = \frac{CF}{Q_g} + \frac{1}{Q_*} \tag{8}$$

The correction factor CF is given for both cases via:

$$\frac{2\sigma_*\sigma_g}{\sigma_*^2+\sigma_g^2} \tag{9}$$

### 3.10 Uncertainty of the Toomre Q parameter measurement

In order to assess the uncertainty of the derived Toomre $Q$ parameter, we propagate our measurement uncertainties, i.e. the final variance of the Toomre $Q_g$ parameter is given by the sum of the following products:

- squared partial derivatives of $Q_g$ with respect to $\kappa$ times the square of the propagated uncertainty of $\kappa$,
- squared partial derivatives of $Q_g$ with respect to $\sigma_g$ times the square of the uncertainty of $\sigma_g$,
- squared partial derivatives of $Q_g$ with respect to $\Sigma_g$ times the squared uncertainty of $\Sigma_g$.

The uncertainty of $Q_*$ is calculated in an analogue way, but with derivatives of $Q_*$ with respect to $\sigma_*$ and $\Sigma_*$ and using the uncertainties on these parameters. For reference, we show the exact formulas we used below:

$$\mathrm{var}(Q_g) = \frac{\sigma_g^2\,\kappa^2\,\mathrm{unc}(\Sigma_g^2)}{\pi^2\,G^2\Sigma_g^4} + \frac{\sigma_g^2\,\mathrm{unc}(\kappa^2)}{\pi^2\,G^2\,\Sigma_g^2} + \frac{\kappa^2\,\mathrm{unc}(\sigma_g^2)}{\pi^2\,G^2\,\Sigma_g^2} \tag{10}$$

$$\mathrm{var}(Q_*) = \frac{\sigma_*^2\,\kappa^2\,\mathrm{unc}(\Sigma_*^2)}{3.36^2\,G^2\Sigma_*^4} + \frac{\sigma_*^2\,\mathrm{unc}(\kappa^2)}{3.36^2\,G^2\,\Sigma_*^2} + \frac{\kappa^2\,\mathrm{unc}(\sigma_*^2)}{3.36^2\,G^2\,\Sigma_*^2} \tag{11}$$

$$\mathrm{var}(\kappa) = \frac{1.9881\ \mathrm{unc}(v(r_{\rm gal}))^2}{r_{\rm gal}^2} \tag{12}$$

[2] https://github.com/astrojohannes/toomreQ

Uncertainty for $Q_* > Q_g$ (gas dominated regime):

$$\mathrm{var}(Q_{\mathrm{tot}}) = \frac{CF^2\ \mathrm{unc}(Q_*)^2}{Q_*^4\ \left(\frac{CF}{Q_*} + \frac{1}{Q_{\mathrm{gas}}}\right)^4} + \frac{\mathrm{unc}(Q_g)^2}{Q_{\mathrm{gas}}^4\ \left(\frac{CF}{Q_*} + \frac{1}{Q_{\mathrm{gas}}}\right)^4} \quad (13)$$

Uncertainty for $Q_* <= Q_g$ (star dominated regime):

$$\mathrm{var}(Q_{\mathrm{tot}}) = \frac{CF^2\ \mathrm{unc}(Q_{\mathrm{gas}})^2}{Q_{\mathrm{gas}}^4\ \left(\frac{CF}{Q_{\mathrm{gas}}} + \frac{1}{Q_*}\right)^4} + \frac{\mathrm{unc}(Q_*)^2}{Q_*^4\ \left(\frac{CF}{\mathrm{gas}} + \frac{1}{Q_*}\right)^4} \quad (14)$$

The individual uncertainties that occur in the equations above are estimated in the following way. Uncertainties of the kinematics parameters derived with $^{3D}$BAROLO are obtained via exploration of the parameter space around the best fit solutions using an MCMC approach (Iorio et al. 2017). Hence, the uncertainties for the gas velocity dispersion, rotation velocity and $\kappa$ should be robust and statistically significant measures.

We stress that asymmetric drift correction is negligible in our case, because the rotation velocities (see Table 2) of LARS 8 are more than ten times higher than the velocity dispersions (de Blok et al. 2008; Iorio et al. 2017). The uncertainties on the final rotation curve are thus equal to the uncertainties of the rotation velocity.

Please refer to the individual sections on gas and stellar masses for a description of how their uncertainties were estimated.

### 3.11 Molecular clumps: identification, virial mass and virial parameter

We apply CPROPSTOO (Williams et al. 1994; Rosolowsky & Leroy 2011; Leroy et al. 2015), an IDL package that is available through GitHub[3] and was developed to identify and measure properties of molecular clouds or clumps in fits data cubes. In particular, CPROPSTOO corrects for the effects of beam convolution and sensitivity when measuring physical properties such as masses or sizes of identified clouds, allowing to make unbiased (beam-independent) measurements. Using a growth-curve analysis on the observed emission line, the algorithm thus extrapolates the measurements to values one would expect in the case of perfect sensitivity. Additionally, CPROPSTOO corrects for finite resolution in both the velocity and spatial domain. This is done via de-convolution of the telescope beam and the width of a spectral channel from the measured cloud size and line width. For more details, we refer the reader to the aforementioned publications. Here we report the main parameters for the `find_local_max` task that we applied for clump identification: delta=2, /snr, minpix=20, minarea=2, minvchan=2, friends=4, specfriends=2.

The virial mass depends on measurements of the size and the observed line width (due to turbulence) of the cloud. If these quantities are known and the radial density profile is given, then following Solomon et al. (1987), the mass of the cloud under the assumptions of virial equilibrium and spherical symmetry can be calculated:

$$M_{\mathrm{vir}} = \frac{3(5-2\gamma)}{G(3-\gamma)} \Delta v^2 R \quad (15)$$

The virial mass $M_{\mathrm{vir}}$ is then given in $\mathrm{M}_\odot$ and depends on the radial density distribution exponent $\gamma$, the linear cloud size (R) in parsec and the full width at half-maximum (FWHM) of the line in km/s ($\Delta$v). Taking the frequently assumed $\gamma$=1 radial density distribution exponent, corresponding to a cloud radial density profile $\rho \propto r^{-1}$ (MacLaren et al. 1988; Hughes et al. 2010), the above equation can be re-written as:

$$M_{\mathrm{vir}} = 1040 \sigma^2 R \quad (16)$$

The units are $\mathrm{M}_\odot$, $\mathrm{km\,s^{-1}}$ and pc for $\mathrm{M_{vir}}$, $\sigma$ and $R$ respectively. In this equation the numerical coefficient accounts for the radial density profile, the conversion factor between FWHM and velocity dispersion ($\Delta$v=2.35$\sigma$) and the gravitational constant. Departures from virial equilibrium can be expressed via the virial parameter, $\alpha_{\mathrm{vir}}$:

$$\alpha_{\mathrm{vir}} = \frac{2K}{U} = \frac{5\sigma^2 R}{G M_{\mathrm{lum}}} = 1.12 \frac{M_{\mathrm{vir}}}{M_{\mathrm{lum}}} \quad (17)$$

where $K$ and $U$ denote the kinetic energy and self-gravitational potential energy respectively. The quantity $\mathrm{M_{lum}}$ is the luminous molecular mass converted from low-J CO intensities using a conversion factor. Virialized clouds without surface pressure or magnetic support have $\alpha_{\mathrm{vir}}$=1, while both marginally bound clouds and clouds in free-fall collapse share energy equipartition ($K = U$) and thus have $\alpha_{\mathrm{vir}}$ ~2 (Ballesteros-Paredes et al. 2011; Camacho et al. 2016; Ibáñez-Mejía et al. 2016; Sun et al. 2018).

### 3.12 Dynamical equilibrium pressure

ISM pressure plays a crucial role in many theories of star formation (e.g. Ostriker & Shetty 2011), as it determines the gas density distribution (Helfer & Blitz 1997; Usero et al. 2015; Bigiel et al. 2016; Gallagher et al. 2018). Following Elmegreen (1989) we estimate the mid-plane dynamic equilibrium pressure, $P_{\mathrm{de}}$, using the following prescription:

$$P_{\mathrm{de}} = \frac{\pi\ G\ \Sigma_{\mathrm{gas}}^2}{2} + \Sigma_{\mathrm{gas}} \sqrt{2\ G\ \rho_*}\ \sigma_{\mathrm{gas}} \quad (18)$$

Here, $\Sigma_{\mathrm{gas}}$ is the total gas surface density, including the atomic and molecular component. Since our study only covers the central part of the galaxy, i.e. the high-density regime, in which most atomic gas is readily converted to molecular gas, we may only consider $\Sigma_{\mathrm{H_2}}$ instead. The vertical velocity dispersion of the gas is denoted as $\sigma_{\mathrm{gas}}$ and the parameter $\rho_*$ is the mass volume density of stars and dark matter at the mid-plane, which we estimate following van der Kruit (1988) using the relation: $\rho_* = \Sigma_*/(2\ h_*)$, with the disc scale height $h_*$. $P_{\mathrm{de}}$ then expresses the pressure needed to balance the vertical gravity on the gas in the galaxy disc. The first term reflects the gas self-gravity, the second term reflects the weight of the gas in the potential well of the stars. Since the stellar potential in LARS 8 exceeds the gas self-gravity, we expect the second term to be dominant.

## 4 RESULTS

The methods outlined in the previous section enable us to quantify clump/cloud properties (Sections 4.1–4.2) as well as star formation relations and radial trends in LARS 8 (Section 4.3). Finally, the gravitational instability of the disc is shown in Section 4.4.

### 4.1 Identification of molecular clumps in LARS 8

Applying CPROPSTOO on our native resolution NOEMA CO (2–1) data cube with a channel width of 10 km/s, we could identify 12 molecular clumps in total (see Figures 6 and 7). The unbiased properties of the identified molecular clumps are summarized in

[3] https://github.com/akleroy/cpropstoo

**Table 3.** Properties of the identified molecular clumps. The clumps in Figures 6 and 7 are identified by the IDs as given in the Table below. See also Equations 16 and 17.

| ID | $R_{\rm eff}$ [pc] | log $M_{\rm lum}$ $M_\odot$ | $\alpha_{\rm vir}$ | $\sigma$ [km s$^{-1}$] | $v_{\rm pos}$ [km s$^{-1}$] |
|---|---|---|---|---|---|
| 1 | 601 | 8.20 | 1.2 | 16.6 | -151 |
| 2 | 322 | 8.14 | 1.0 | 19.2 | -126 |
| 3 | 913 | 8.55 | 0.9 | 16.8 | -135 |
| 4 | 343 | 8.59 | 1.0 | 30.7 | -92 |
| 5 | 340 | 9.23 | 0.8 | 59.7 | -73 |
| 6 | 320 | 8.40 | 1.4 | 31.1 | -63 |
| 7 | 1023 | 9.26 | 0.5 | 27.8 | 4 |
| 8 | 469 | 8.51 | 1.7 | 32.0 | 53 |
| 9 | 436 | 8.76 | 1.1 | 34.5 | 56 |
| 10 | 609 | 8.89 | 0.4 | 20.5 | 135 |
| 11 | 480 | 8.57 | 1.0 | 26 | 164 |
| 12 | 436 | 8.21 | 1.9 | 24.7 | 181 |

Table 3. Their masses range from $10^{8.1}$ to $10^{9.3}$ $M_\odot$, covering linear (extrapolated) diameters between ~600–2000 pc. Clump 7 was found to be the most massive one, located in the very center of the galaxy. The channel maps between approximately $-180$ km s$^{-1}$ and $+210$ km s$^{-1}$ in Figure 7 may suggest that `CPROPSTOO` failed in associating extended gas to clumps in the central region of the galaxy. This is because the linewidth in the central few pixels of the galaxy is extremely wide (more than 300 km$^{-1}$) due to beam smearing. Much higher resolution (spatially and spectrally) would be needed to identify individual clumps in that part of the galaxy.

### 4.2 Mass-size relation for the massive clumps

Figure 8 compares the derived masses and sizes of the molecular clumps identified in LARS 8 to the literature compilation of Nguyen-Luong et al. (2016), which contains giant molecular clouds (GMCs) of the Milky Way with sizes smaller than 10 pc, molecular cloud complexes (MCCs) with sizes between 10 and 1000 pc, as well as galaxies and structures larger than 1 kpc typically found at high redshift. Note that the identified structures or clumps in LARS 8 are resolved, i.e. their deconvolved diameters are at least as wide as the beam major axis. We thus conclude from Figure 8 that the clumps of diffuse molecular gas in LARS 8 are in fact scaled-up versions of the MCCs in the literature. In the mass-size relation they populate the range between MCCs and structures identified at high redshifts. However – despite an ongoing massive star formation process in LARS 8 – the clumps follow the same trend between mass and size. This finding implies a universal (constant) diffuse molecular mass surface density, even in highly star-forming galaxies such as LARS 8. The elevated star formation rates must thus result from processes *within* the large diffuse molecular reservoirs we identified in CO (2–1). It might be that either the structures contain more over-densities (e.g. traced by HCN) or that the star formation is in some way more efficient. The latter is supported by observations of Messa et al. (2019), who have derived sizes and properties of clumps identified from very high-resolution UV photometry. They find that the range of clump sizes in LARS 8 is similar to those in normal star forming galaxies or at high redshift, i.e. 15–200 pc. However, the star formation rates per UV clump are higher and fall between those observed in the local and high-$z$ Universe. Also, a combination of both more dense clumps and higher efficiency per clump may apply.

### 4.3 Radial profiles and KS relation

Figure 9 shows inclination-corrected, elliptical profiles of several quantities we have derived, centered on the maximum stellar surface density. The plots show that while the molecular gas surface density declines relatively smoothly from the center outwards, the stellar surface density is peaked in the innermost ~500 pc. This peak may represent a bulgelike structure that is about to form, similar to observations in high redshift discs (Elmegreen et al. 2009) and as predicted by numerical simulations, e.g. in Elmegreen et al. (2008). Thereby, gas-rich disc galaxies show disc instabilities that first trigger clump formation. These clumps (and other disc matter) move inwards and merge, forming a bulge (or bulgelike-clump) that is characterized by a Sersic index n=4 (like a classical bulge) and rotation. See Rasekh et al. (2022) for a compilation of Sersic profiles for LARS galaxies.

In contrast, the star formation rate density is highest in a ring-like structure located at a radius of ~1.2 kpc. The lowering of the SFR towards the inner kiloparsec in combination with the low molecular gas fraction suggests that some process has quenched star formation in the center, e.g. AGN feedback. Alternatively, it might be that the extinction correction underestimates the true SFRs in the innermost parts, where Hα becomes optically thick. However, this would not explain the relatively low gas fraction in the center.

Moreover, Figure 9 reveals that the molecular gas depletion time, $\tau_{\rm depl}$, strongly declines from more than 1 Gyr in the center to ~100 Myr in the outer parts of the disc. This contrasts normal star-forming galaxies that typically have roughly constant (Bigiel et al. 2011) or even radially increasing gas depletion time scales (Leroy et al. 2008). This behaviour is further suggested by (some) gravity-driven theoretical models of star formation, e.g. Krumholz et al. (2012) argue that in the regime of normal star-formation the GMCs are basically decoupled from the rest of the ISM. The depletion time is then mainly set by the internal properties and processes of the GMCs – that are roughly constant in normal Milky-Way-like clouds – rather than by the large-scale behavior of the ISM. Krumholz et al. (2012) further argue that in starbursts (with a Toomre $Q$ parameter ~1) the depletion time should be set by the orbital (dynamical) time. However, given the fact that the orbital time increases with radius (flat rotation) one would expect from such theory that the depletion time increases with radius. This is not observed in LARS 8.

The molecular Kennicutt-Schmidt relation for LARS 8 is presented in Figure 10. Each point in the plot represents an independent measurement (line-of-sight) that we calculated from the mean value within 2x2 bins (using `numpy reshape`). It is seen that the measurements of individual lines-of-sight exhibit a relatively large scatter within a range of roughly one order of magnitude. However, the central region forms an interesting feature that is characterised by a roughly constant star formation rate density while the molecular gas surface density varies by up to an order of magnitude, with a mean gas depletion time around ~1 Gyr.

### 4.4 Disc stability - Toomre $Q$ analysis

Using the smoothed rotation curve (see Figure 4) derived from the NOEMA CO (2–1) data cube, and subsequent calculation of the $\beta$-parameter and the epicyclic frequency $\kappa$, the Toomre $Q$ parameters for the molecular gas ($Q_{\rm gas}$), the stellar component ($Q_*$) and the combined total instability parameter ($Q_{\rm tot}$) could be computed as a function of galactocentric radius (see Figure 11). Note that we have centered the previously discussed radial profiles on the stellar peak, while here we (have to) use the kinematic center. Between these

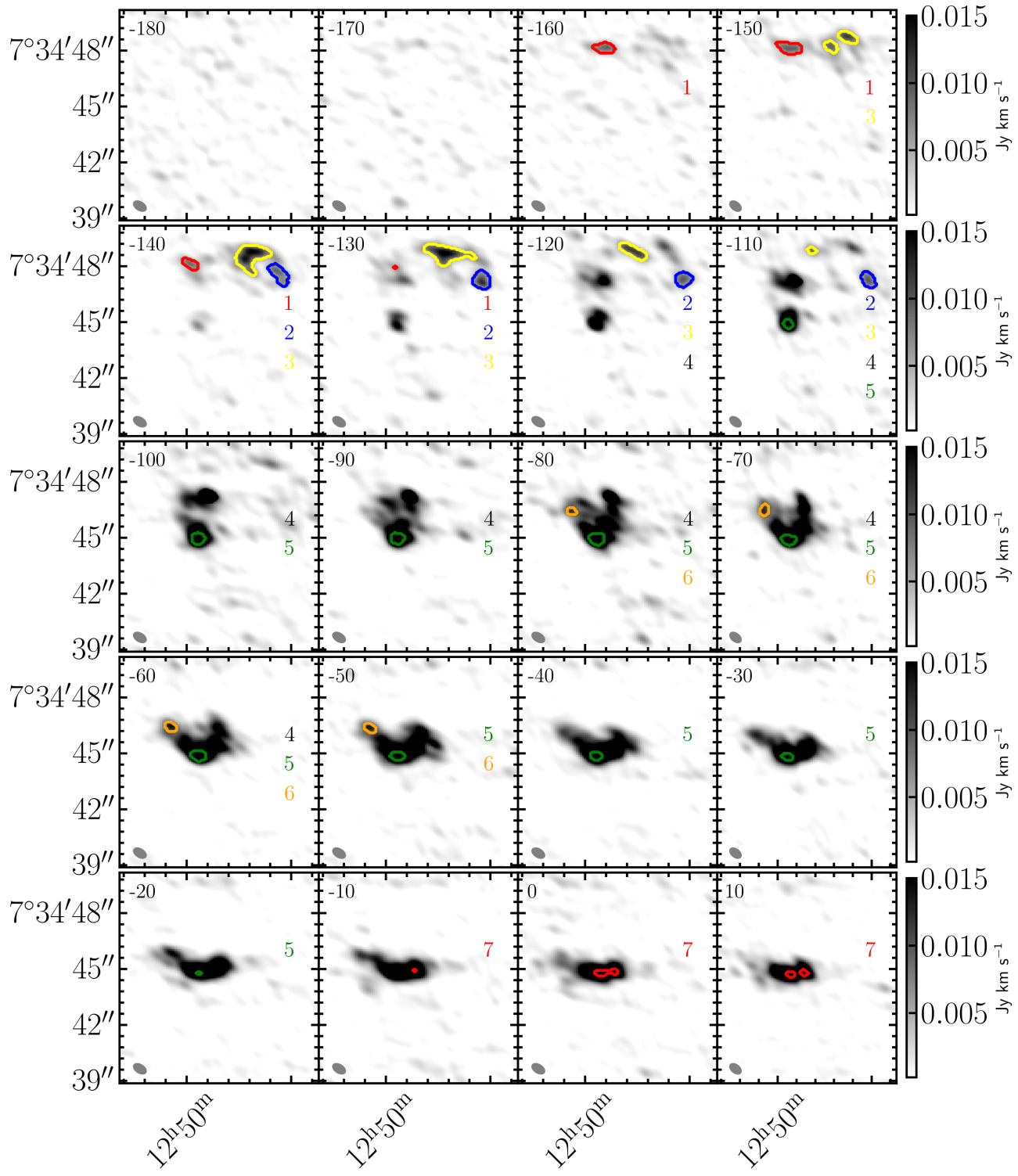



**Figure 6.** NOEMA CO (2–1) channel maps of the northern part of LARS 8, showing velocities between -180 and +10 km/s with identified CPROPSTOO structures (shown as contours). Properties of the identified clumps are summarized in Table 3.

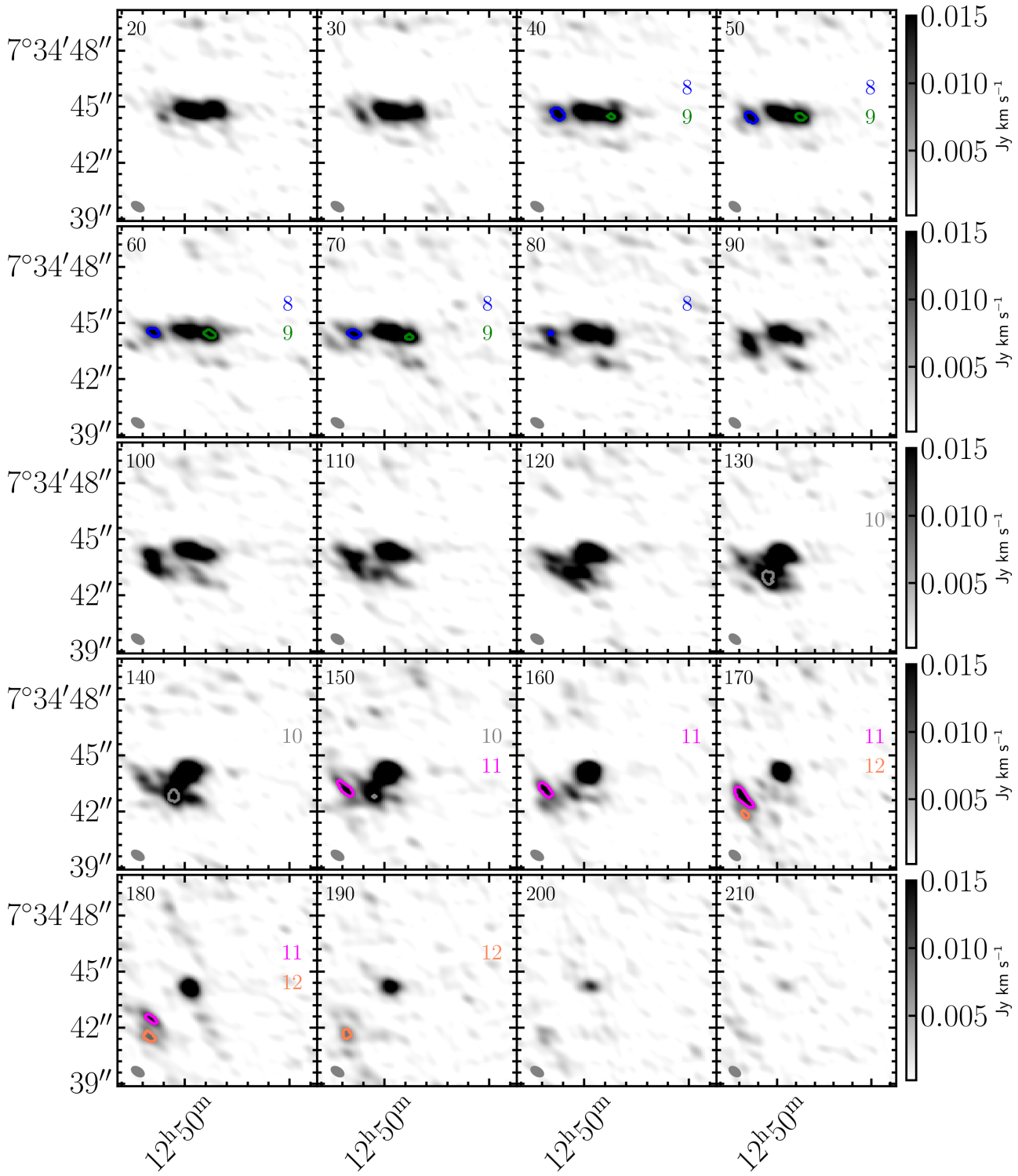



**Figure 7.** NOEMA CO (2–1) channel maps of the southern part of LARS 8, showing velocities between 20 and +210 km/s with identified CPROPSTOO structures (shown as contours). Properties of the identified clumps are summarized in Table 3.

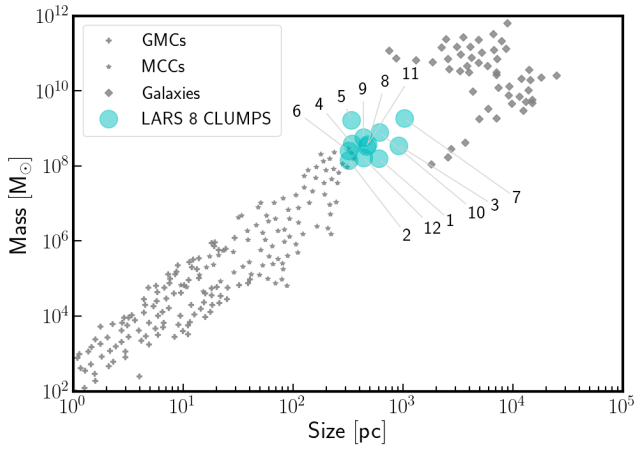



**Figure 8.** Mass-size relation for the massive clumps identified in LARS 8 (*cyan points*) with the ID numbers as given in Table 3. The clumps are compared to the literature compilation of Nguyen-Luong et al. (2016), that is based on GMC (*plus signs*) data of Onishi et al. (2002); Heyer et al. (2009); Maruta et al. (2010); Roman-Duval et al. (2010); Evans et al. (2014); Shimajiri et al. (2015), MCC (*stars*) data of Rosolowsky (2007); Murray (2011); Wei et al. (2012); Miura et al. (2012, 2014); Donovan Meyer et al. (2013); García et al. (2014) and galaxies (*diamonds*) from Leroy et al. (2013); Tacconi et al. (2013); Genzel et al. (2010).

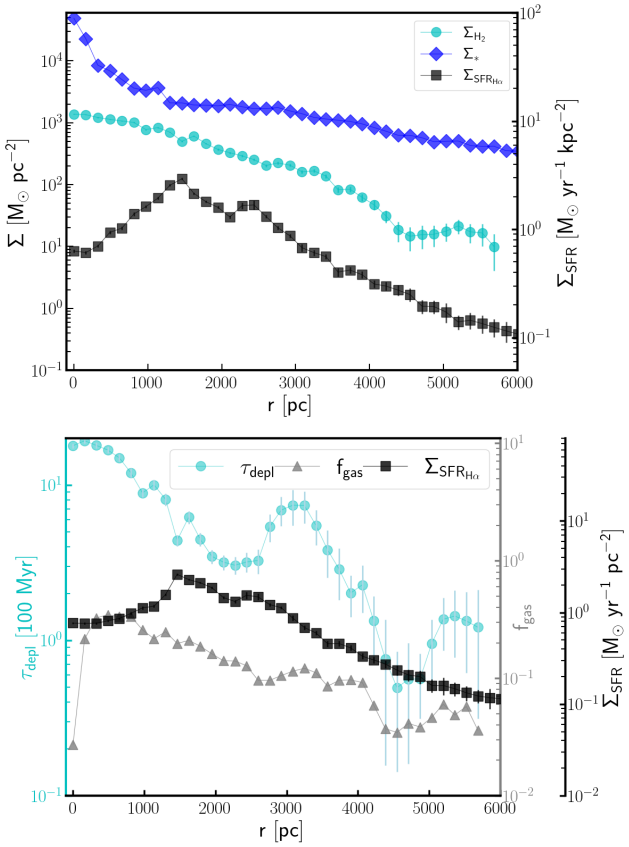



**Figure 9.** *Top panel*: Elliptical inclination-corrected profiles of stellar (*blue diamonds*), molecular (*cyan circles*) and SFR surface densities (*black squares*). *Bottom panel*: Same as top panel for the molecular gas depletion time ($\tau_{depl}$), the Hα-based star formation rate surface density ($\Sigma_{SFR}$) and the molecular gas fraction ($f_{gas}$).

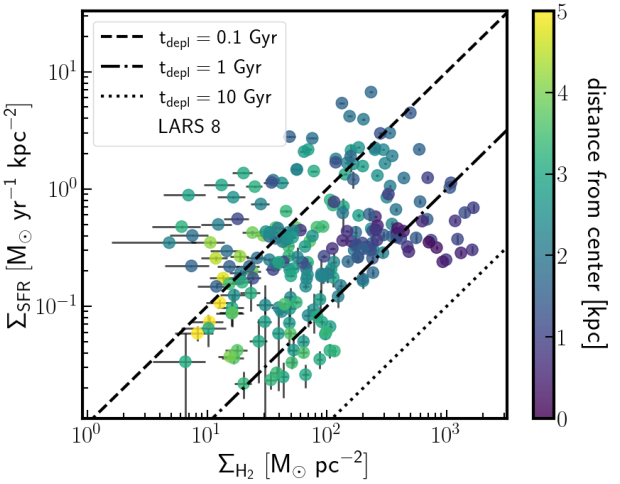



**Figure 10.** Resolved molecular Kennicutt-Schmidt relation for LARS 8, based on SFRs from extinction-corrected Hα and molecular masses from CO (2–1), both corrected for inclincation. Each point corresponds to a measurement in a ~650 pc sized region/pixel. The colors indicate distance from the center.

two we find an offset of ~0.8 arcsec or ~650 pc. Such offset is also found in numerical simulations of Elmegreen et al. (2008) during the phase of the formation of a central bulgelike-clump. We stress that the overall shape of the radial profiles does not change if the kinematic center is used instead.

Figure 11 reveals that only the innermost ~500 pc of LARS 8 are stable. This central stability is mainly driven by high values of $\kappa$ due to the extremely steep rise in rotation velocity that causes very high $\beta$ values. Note that although we cannot (kinematically) resolve the central ~500 pc, i.e. we cannot distinguish between rotation and dispersion (beam smearing), it is still possible to compute $\kappa$. The plot further shows that the outskirts of the disc are unstable over large scales, with values of $Q_{tot}$ well below the critical limit of 1. Such highly unstable discs are not observed in normal star-forming disc galaxies (Leroy et al. 2008), but seem typical for the clumps observed in massive high-$z$ discs (Genzel et al. 2011; Wisnioski et al. 2012; Mieda et al. 2016). The relatively high star formation rate surface densities observed in LARS 8 over large scales are thus likely the result of enhanced disc fragmentation due to $Q_{tot}$ <<1. These instabilities thus trigger the formation of massive stellar and molecular clumps.

However, it seems that purely gravity-driven theoretical models of star formation do not reproduce our observations, in particular e.g. Krumholz et al. (2012) predict for galaxies in the Toomre regime (as LARS 8) a positive correlation between the molecular gas depletion time and the orbital period. As explained, this is not observed in LARS 8.

Other models assume that the star formation process is self-regulated and thus leads to pressure balance in the ISM. In particular, the star-forming system is then in balance between feedback processes from star formation and the external pressure. In case of a disc galaxy the relevant pressure is then $P_{de}$, the dynamical equilibrium pressure. Based on that, e.g. Ostriker & Shetty (2011) predict a linear relation between the star formation rate surface density and the ISM pressure. We test this prediction in the next section.

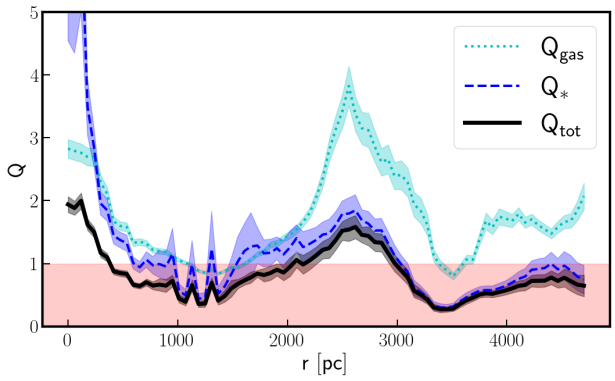



**Figure 11.** LARS 8 disc stability from radial Toomre $Q$ analysis. Regions with $Q$ <1 (*light red shaded area*) are considered unstable. The total instability parameter ($Q_{\rm tot}$) is shown as *black* curve with the *grey shaded area* indicating its uncertainty. The contribution of the stellar and the gaseous component are shown by the *blue* and *cyan* curves respectively.

## 5 DISCUSSION

We showed in the previous section that the galactic disc of LARS 8 is highly unstable, in particular at radii outwards of ~500 pc. The Toomre $Q$ parameter is found to be significantly lower than one (see Figure 11) and we conclude that the formation of the observed massive molecular and stellar clumps is driven by fragmentation of the disc rather than accretion of external mass or merging. Contrarily, the central region of LARS 8 was found to be different. It has a Toomre $Q$ parameter greater than one and is thus stable, it has a relatively low gas fraction and a low star formation rate density, and it has a depletion time of more than ~1 Gyr (which is much longer than within the disc).

Utomo et al. (2017) studied the molecular gas depletion time as a function of local environment in 52 non-AGN disc galaxies drawn from the EDGE-CALIFA (Sánchez et al. 2012; Bolatto et al. 2017) survey. They find that galaxies with increased central stellar surface densities (relative to the disc) typically show a decrease in $\tau_{\rm depl}$ in the center. As stellar surface density is the determining factor for ISM pressure, Utomo et al. (2017) claim that the observed shorter central gas depletion times are a consequence of higher external pressure that facilitates cloud collapse. In the center of LARS 8 we also observe an increase in stellar surface density compared to the disc, but at the same time – for the center – we find *longer* molecular gas depletion times. Additionally, our radial plots (Figure 9) show that the star formation rate surface density sharply drops towards the center, while the molecular gas surface density in LARS 8 decreases relatively smoothly from the center to the outskirts.

Some process in the center must therefore lead to quenching of star formation. We find evidence that shear is mainly responsible for the suppression of star formation in the center, as we see that $\kappa$ increases by a factor of ~4 between a radius of ~1 kpc towards the innermost central region. Also the gas velocity dispersion increases in that radial regime (from ~1 kpc to the center), however only by roughly 50 percent. Thus, it is mainly shear that causes $Q >> 1$ in the center. Feedback from supernovae (that drive the gas velocity dispersion) thus plays only a minor role (if any) for the suppression of star formation. In fact our kinematic results (see Table 2) even suggest that the gas velocity dispersion drops towards the innermost region. This observation further rules out feedback from SNe, but we caution that the measurement of velocity dispersion in the center is relatively uncertain due to beam smearing caused by the steep increase of the rotation curve. However, further support against star formation quenching due to SNe is found from stellar population synthesis performed by Melinder et al (in preparation). They show that the central ~500 pc of LARS 8 are dominated by old stars with ages >1 Gyr.

We also compare our observations to the feedback models of e.g. Ostriker et al. (2010) or Faucher-Giguère et al. (2013), which are based on a balance between energy injected through feedback and disc vertical pressure. The models predict an inverse relation between $\tau_{\rm depl}$ and the vertical gas velocity dispersion. Such relation was previously observed by Fisher et al. (2019) in a set of massive and highly turbulent discs. However, from our data of the central region of LARS 8 we cannot test any such correlation, because of spatial resolution and beam smearing that makes measurements of the velocity dispersion extremely challenging.

Given our current data, we thus conclude that shear is the most likely cause for the relatively low star formation rates in the center and the long depletion times. As we mentioned in the previous section, it might also be the case that the computed star formation rates in the center are somewhat spurious due to the relatively high extinction found in this region. We stress that the total galaxy-wide SFR from extinction-corrected Hα is in fact 50 percent higher than the SFR we previously derived in Puschnig et al. (2020) from far infrared measurements. This might be an indication that the Balmer-decrement method overestimates the true fluxes/SFRs rather than underestimating it. On the other hand, the discrepancy between infrared and Hα based SFRs may be the result of a star formation history with a recent burst (to which Hα is more sensitive).

In contrast, the environmental properties of the outer disc of LARS 8 are different, in particular we find that the disc is highly unstable. The radial profiles in Figure 9 further revealed that the molecular gas depletion time in LARS 8 decreases with the galactic radius. This behaviour is contrary to what is typically observed in nearby disc galaxies in which $\tau_{\rm depl}$ either stays flat or slightly increases with radius (Leroy et al. 2008). Note that models of star formation in stable discs, e.g. Krumholz et al. (2012), predict exactly such behaviour for GMCs that are basically decoupled from the large-scale ISM. In these models star formation is mainly dictated by local properties rather than large-scale effects. Additionally, Semenov et al. (2017) showed that for regular, local spiral galaxies, $\tau_{\rm depl}$ is ~1–2 Gyr due to the long time the gas spends in the non-star-forming phase, while only a small fraction of the gas is converted into stars within a short time.

The difference in the radial $\tau_{\rm depl}$ profiles between LARS 8 and normal star forming disc galaxies (Romeo & Mogotsi 2017) is thus the result of the observed large-scale Toomre instabilities in LARS 8, in which the ISM is dominated by dozens of supermassive star-forming clouds that disallow the star forming regions to decouple from the ambient ISM (as they make up the ISM). Krumholz et al. (2012) also made predictions of $\tau_{\rm depl}$ for starbursts in the Toomre regime ($Q$ ~1), for which they find that $\tau_{\rm depl}$ should mainly be dictated by the dynamic timescale, i.e. $2r\pi/v_{\rm rot}$. Our observations, however, are not in agreement with this prediction of a radially increasing gas depletion time. We argue that the observed instabilities in LARS 8 are more violent ($Q$ <<1) and thus involve more complex physical processes such as galaxy-scale shocks or inflows (Barnes 2004; Teyssier et al. 2010; Powell et al. 2011) which were omitted by the models of Krumholz et al. (2012).

We now test our observations against models that are based on the assumption that star formation is self-regulated through a

balance between ISM pressure and feedback. For example, Ostriker & Shetty (2011) and Kim et al. (2013) predict in their semi-analytic models a (nearly) linear relationship between the pressure and the star formation rate surface density: $\Sigma_{\rm SFR} = 4\ f^{-1}\ P_{\rm de}$. As described in Fisher et al. (2019) the scaling factor $f$ can be determined from $\sigma_{\rm gas} = 0.366\ (\tau_{\rm ff}/\tau_{\rm depl})\ f$ (Shetty & Ostriker 2012). This leaves the free-fall timescale $\tau_{\rm ff}$ as the only unknown. Krumholz et al. (2012) further estimate that the range of $\tau_{\rm ff}$ should be between 1–10 Myr for starburst galaxies, i.e. in high density regimes. In Figure 12 we plot the star formation rate densities against pressure for LARS 8 and two comparison samples. Each point in the plot represents an independent measurement (line-of-sight) that we calculated from the mean value within 2x2 bins. The dashed and dotted lines indicate the model predictions for the above mentioned range in $\tau_{\rm ff}$ and a fixed gas depletion time of 300 Myr that we typically find in the disc of LARS 8. The Figure shows that the predicted linear relation does not fit the data, we rather find evidence for a sub-linear trend, similar to Fisher et al. (2019). The slope in LARS 8, however, seems even shallower, in particular in the low-pressure regime. We conclude that in the outskirts of the observed disc the star formation is out of equilibrium as described in feedback-regulated star formation models, and is dictated by large scale instabilities instead.

The importance of the large-scale environment for star formation in LARS 8 is also reflected by the fact that the virial parameter of the identified diffuse molecular structures (see Table 3) has values that are roughly identical to those found in Milky Way GMCs or normal disc galaxies (Sun et al. 2018). Most clumps are found to be virialized with $\alpha_{\rm vir} \sim 1$ in which kinetic and gravitational energy are roughly balanced. This provides further evidence that on the scale of a few hundred parsec the stars form in a roughly uniform environment. The high star formation rates observed in LARS 8 must thus be caused by an increase in the number of clouds that are triggered by large-scale gravitational instability (with low Toomre $Q$). Hence, the shorter gas depletion time scale – or higher star formation efficiency – observed in the outer disc does not imply that on our clump scales the process of star formation is more efficient, but rather that the formation of individual clumps is more efficient.

Next, we discuss how the choice of a fixed CO conversion factor $\alpha_{\rm CO}$ impacts our findings of the radial trend of $\tau_{\rm depl}$ and the Toomre $Q$ instability of the disc. We know from the MUSE data that there is a slight increase in metallicity towards the center of the galaxy. Hence, application of a metallicity-dependent conversion factor would only lead to a relatively lower value of $\alpha_{\rm CO}$ in the center than in the outer part of the disc. As a result, this would only exaggerate the observed trend of decreasing molecular gas depletion with radius. For the results of our disc stability analysis, the fixed conversion factor has only minor impacts for two reasons. First, the instabilities are mainly driven by the stellar component (which is formally also shown in Romeo & Falstad 2013). Second, it would only lead to slightly higher gas surface densities in the disc, lowering support of the disc against collapse and thus resulting in even lower $Q$ values.

However, not only the metallicity impacts the conversion factor. In infrared galaxies, but also in the centers of nearby galaxies, the nuclear zone is sometimes found to have lower $\alpha_{\rm CO}$ caused by hotter molecular gas, thus higher velocity dispersion (which reduces the CO optical depth). This is seen e.g. in NGC 6946 (Meier & Turner 2004). If CO optical depths in the center of LARS 8 were systematically lower, we would need to use a lower conversion factor. In the case of a typical ULIRG value ($\alpha_{\rm CO} \sim 1$), the central depletion time would then drop from 1.35 Gyr to 300 Myr. At the same time, this would provide even further support against collapse in the central zone. We plan to resolve this issue with observations of CO isotopologues in a future study.

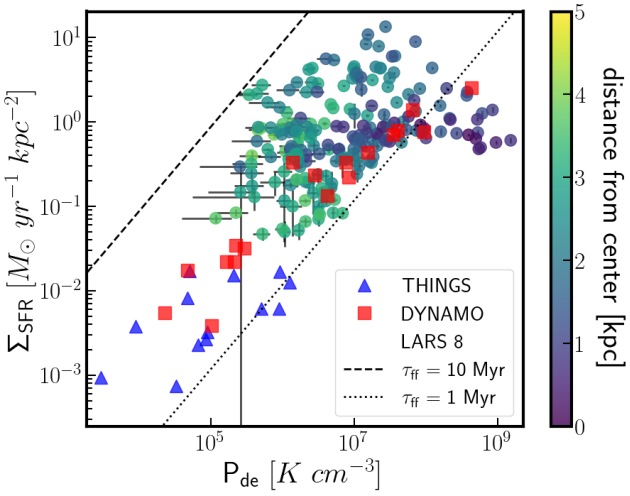



**Figure 12.** Star formation rate surface density (y-axis) versus dynamical equilibrium pressure (x-axis). Each point corresponds to a measurement in a ~650 pc sized region/pixel. The colors indicate the distance from the center.

## 6 SUMMARY AND CONCLUSION

We have obtained new high-resolution NOEMA CO (2–1) and MUSE spectroscopy of the $z$ ~0 massive, clumpy and gas-rich disc galaxy LARS 8, drawn from the *Lyman Alpha Reference Sample*. The NOEMA data was used to study the diffuse molecular gas content and its kinematics at a resolution of ~400 pc, while the MUSE data was used to derive extinction-corrected star formation rates from Hα at a resolution of ~600 pc. This enabled us – together with readily available HST photometry – to perform a disc stability analysis using the Toomre $Q$ criterion. The main result is presented in Figure 11, showing that the disc is highly unstable ($Q$ <<1) over large scales. On the other hand, the center of LARS 8 was found to be stable ($Q$ >1).

The NOEMA molecular data cube was further examined with CPROPSTOO, allowing us to identify and compute physical properties of 12 individual molecular clumps (Table 3). The clumps are found to be virialized ($\alpha_{\rm vir}$ ~1) and they follow the mass-size relation (Figure 8).

We have further derived several physical parameters such as the molecular gas depletion time, the molecular gas fraction and the dynamical equilibrium pressure. Using our results from the CO-based rotation curve (Figure 4), all (surface) quantities could be corrected for inclination effects. The radial (elliptical) profiles are shown in Figure 9. Of particular interest is the smooth radial decline of the molecular gas depletion time, ranging from more than 1 Gyr in the center to ~100 Myr in the outer disc. This trend is outstanding, as in normal star forming galaxies the gas depletion time is observed to be constant or even slightly increasing with radius. These results lead to the following conclusions:

- The disc of LARS 8 is highly unstable with $Q$ <<1 and has relatively short gas depletion times. The identified diffuse molecular structures, however, are virialized and thus similar to GMCs in the

Milky Way or nearby galaxies. Hence, the short gas depletion times in the disc cannot be explained by local (sub-kpc) effects such as a higher local star formation efficiency, but must be triggered by large-scale processes that cause the formation of more massive and *denser* molecular clumps. The observed short gas depletion times observed in the disc must thus result from more dense gas being present on sub-clump scales, i.e. density PDFs shifted towards higher values. We argue that the high star formation rates observed in LARS 8 are the result of large-scale Toomre instabilities in the galaxy disc.

- The central region of LARS 8 is Toomre-stable, has the longest gas depletion time, lower gas fraction and a reduced star formation rate surface density. Given the fact that the stellar surface density (and thus the ISM pressure) is found to be highest in the center, we argue that some process must lower star formation in the central ~500 pc. From our dynamical analysis we find evidence that shear (and not feedback from SNe) is the main driving mechanism that suppresses the star formation in the center of LARS 8, as $\kappa$ increases by a factor of 4 from r~1 kpc to r~0 kpc.

## ACKNOWLEDGEMENTS

J.P. acknowledges funding from the European Research Council (ERC) under the European Union's Horizon 2020 research and innovation programme (grant agreement No.726384/Empire). M.H. is Fellow of the Knut and Alice Wallenberg Foundation. O.A. acknowledges support from the Knut and Alice Wallenberg Foundation and from the Swedish Research Council (grant 2019-04659). This research made use of Astropy, a community-developed core Python package for Astronomy (Astropy Collaboration et al. 2013).

## DATA AVAILABILITY

The MUSE raw data underlying this article are available in the ESO public archive at http://archive.eso.org/ and can be accessed with the program ID 0101.B-0703(A). The reduced MUSE data cube and the NOEMA data underlying this article will be shared on reasonable request to the corresponding author.

## REFERENCES

Agertz O., Lake G., Teyssier R., Moore B., Mayer L., Romeo A. B., 2009a, MNRAS, 392, 294
Agertz O., Teyssier R., Moore B., 2009b, MNRAS, 397, L64
Astropy Collaboration et al., 2013, A&A, 558, A33
Bacon R., et al., 2010, in McLean I. S., Ramsay S. K., Takami H., eds, Society of Photo-Optical Instrumentation Engineers (SPIE) Conference Series Vol. 7735, Ground-based and Airborne Instrumentation for Astronomy III. p. 773508, doi:10.1117/12.856027
Ballesteros-Paredes J., Hartmann L. W., Vázquez-Semadeni E., Heitsch F., Zamora-Avilés M. A., 2011, MNRAS, 411, 65
Barnes J. E., 2004, MNRAS, 350, 798
Behrendt M., Burkert A., Schartmann M., 2015, MNRAS, 448, 1007
Belfiore F., et al., 2022, A&A, 659, A26
Bigiel F., et al., 2011, ApJ, 730, L13
Bigiel F., et al., 2016, ApJ, 822, L26
Bittner A., et al., 2019, A&A, 628, A117
Bolatto A. D., Wolfire M., Leroy A. K., 2013, ARA&A, 51, 207
Bolatto A. D., et al., 2017, ApJ, 846, 159
Bournaud F., et al., 2012, ApJ, 757, 81
Brinchmann J., Charlot S., White S. D. M., Tremonti C., Kauffmann G., Heckman T., Brinkmann J., 2004, MNRAS, 351, 1151
Calzetti D., Liu G., Koda J., 2012, ApJ, 752, 98
Camacho V., Vázquez-Semadeni E., Ballesteros-Paredes J., Gómez G. C., Fall S. M., Mata-Chávez M. D., 2016, ApJ, 833, 113
Cappellari M., 2017, MNRAS, 466, 798
Cappellari M., Emsellem E., 2004, PASP, 116, 138
Cardelli J. A., Clayton G. C., Mathis J. S., 1989, ApJ, 345, 245
Cassata P., et al., 2020, ApJ, 891, 83
Ceverino D., Klypin A., 2009, ApJ, 695, 292
Chabrier G., 2003, PASP, 115, 763
Daddi E., et al., 2007, ApJ, 670, 156
Dekel A., Sari R., Ceverino D., 2009, ApJ, 703, 785
Dessauges-Zavadsky M., Adamo A., 2018, MNRAS, 479, L118
Dessauges-Zavadsky M., et al., 2017, A&A, 605, A81
Dessauges-Zavadsky M., et al., 2019, Nature Astronomy, 3, 1114
Di Teodoro E. M., Fraternali F., 2015, MNRAS, 451, 3021
Donovan Meyer J., et al., 2013, ApJ, 772, 107
Elbaz D., et al., 2007, A&A, 468, 33
Elbaz D., et al., 2018, A&A, 616, A110
Elmegreen B. G., 1989, ApJ, 338, 178
Elmegreen B. G., Bournaud F., Elmegreen D. M., 2008, ApJ, 688, 67
Elmegreen B. G., Elmegreen D. M., Fernandez M. X., Lemonias J. J., 2009, The Astrophysical Journal, 692, 12
Emsellem E., et al., 2022, A&A, 659, A191
Evans II N. J., Heiderman A., Vutisalchavakul N., 2014, ApJ, 782, 114
Faucher-Giguère C.-A., Quataert E., Hopkins P. F., 2013, MNRAS, 433, 1970
Fisher D. B., et al., 2014, ApJ, 790, L30
Fisher D. B., et al., 2017, ApJ, 839, L5
Fisher D. B., Bolatto A. D., White H., Glazebrook K., Abraham R. G., Obreschkow D., 2019, The Astrophysical Journal, 870, 46
Förster Schreiber N. M., et al., 2009, ApJ, 706, 1364
Gallagher M. J., et al., 2018, ApJ, 858, 90
García P., Bronfman L., Nyman L.-Å., Dame T. M., Luna A., 2014, ApJS, 212, 2
Genzel R., et al., 2006, Nature, 442, 786
Genzel R., et al., 2008, ApJ, 687, 59
Genzel R., et al., 2010, MNRAS, 407, 2091
Genzel R., et al., 2011, ApJ, 733, 101
Genzel R., et al., 2015, ApJ, 800, 20
Hayes M., et al., 2014, ApJ, 782, 6
Helfer T. T., Blitz L., 1997, ApJ, 478, 233
Herenz E. C., et al., 2016, A&A, 587, A78
Heyer M., Krawczyk C., Duval J., Jackson J. M., 2009, ApJ, 699, 1092
Högbom J. A., 1974, A&AS, 15, 417
Hughes A., et al., 2010, MNRAS, 406, 2065
Ibáñez-Mejía J. C., Mac Low M.-M., Klessen R. S., Baczynski C., 2016, ApJ, 824, 41
Iorio G., Fraternali F., Nipoti C., Di Teodoro E., Read J. I., Battaglia G., 2017, MNRAS, 466, 4159
Kim C.-G., Ostriker E. C., Kim W.-T., 2013, ApJ, 776, 1
Kregel M., van der Kruit P. C., de Grijs R., 2002, MNRAS, 334, 646
Krumholz M. R., Burkhart B., 2016, MNRAS, 458, 1671
Krumholz M. R., Dekel A., McKee C. F., 2012, ApJ, 745, 69
Le Reste A., et al., 2022, ApJ, 934, 69
Lehnert M. D., Nesvadba N. P. H., Le Tiran L., Di Matteo P., van Driel W., Douglas L. S., Chemin L., Bournaud F., 2009, ApJ, 699, 1660
Leroy A. K., Walter F., Brinks E., Bigiel F., de Blok W. J. G., Madore B., Thornley M. D., 2008, AJ, 136, 2782
Leroy A. K., et al., 2013, AJ, 146, 19
Leroy A. K., et al., 2015, ApJ, 801, 25
MacLaren I., Richardson K. M., Wolfendale A. W., 1988, ApJ, 333, 821
Madau P., Dickinson M., 2014, ARA&A, 52, 415
Mandelker N., Dekel A., Ceverino D., DeGraf C., Guo Y., Primack J., 2017, MNRAS, 464, 635
Maruta H., Nakamura F., Nishi R., Ikeda N., Kitamura Y., 2010, ApJ, 714, 680
Meier D. S., Turner J. L., 2004, AJ, 127, 2069
Messa M., Adamo A., Ã-stlin G., Melinder J., Hayes M., Bridge J. S., Cannon J., 2019, MNRAS, 487, 4238

Micheva G., et al., 2018, A&A, 615, A46
Mieda E., Wright S. A., Larkin J. E., Armus L., Juneau S., Salim S., Murray N., 2016, ApJ, 831, 78
Miura R. E., et al., 2012, ApJ, 761, 37
Miura R. E., et al., 2014, VizieR Online Data Catalog, p. J/ApJ/761/37
Moody C. E., Guo Y., Mandelker N., Ceverino D., Mozena M., Koo D. C., Dekel A., Primack J., 2014, MNRAS, 444, 1389
Murray N., 2011, ApJ, 729, 133
Nguyen-Luong Q., et al., 2016, ApJ, 833, 23
Noeske K. G., et al., 2007, ApJ, 660, L47
Oklopčić A., Hopkins P. F., Feldmann R., Kereš D., Faucher-Giguère C.-A., Murray N., 2017, MNRAS, 465, 952
Onishi T., Mizuno A., Kawamura A., Tachihara K., Fukui Y., 2002, ApJ, 575, 950
Östlin G., et al., 2014, ApJ, 797, 11
Ostriker E. C., Shetty R., 2011, ApJ, 731, 41
Ostriker E. C., McKee C. F., Leroy A. K., 2010, ApJ, 721, 975
Pardy S. A., et al., 2014, ApJ, 794, 101
Peng Y.-j., et al., 2010, ApJ, 721, 193
Pietrinferni A., Cassisi S., Salaris M., Castelli F., 2004, ApJ, 612, 168
Popesso P., et al., 2019, MNRAS, 483, 3213
Powell L. C., Slyz A., Devriendt J., 2011, MNRAS, 414, 3671
Puech M., 2010, MNRAS, 406, 535
Puschnig J., 2020, Galactic Disc Stability Analyzer (Toomre Q), doi:10.5281/zenodo.3657258, https://doi.org/10.5281/zenodo.3657258
Puschnig J., et al., 2020, A&A, 644, A10
Rasekh A., et al., 2022, A&A, 662, A64
Rodighiero G., et al., 2011, ApJ, 739, L40
Rodrigues M., Hammer F., Flores H., Puech M., Athanassoula E., 2017, MNRAS, 465, 1157
Roman-Duval J., Jackson J. M., Heyer M., Rathborne J., Simon R., 2010, ApJ, 723, 492
Romeo A. B., Agertz O., 2014, MNRAS, 442, 1230
Romeo A. B., Falstad N., 2013, MNRAS, 433, 1389
Romeo A. B., Mogotsi K. M., 2017, MNRAS, 469, 286
Rosolowsky E., 2007, ApJ, 654, 240
Rosolowsky E., Leroy A., 2011, CPROPS: Bias-free Measurement of Giant Molecular Cloud Properties (ascl:1102.012)
Safronov V. S., 1960, Annales d'Astrophysique, 23, 979
Saintonge A., et al., 2017, ApJS, 233, 22
Sánchez S. F., et al., 2012, A&A, 538, A8
Scoville N., et al., 2017, ApJ, 837, 150
Semenov V. A., Kravtsov A. V., Gnedin N. Y., 2017, ApJ, 845, 133
Shapiro K. L., Gerssen J., van der Marel R. P., 2003, AJ, 126, 2707
Shetty R., Ostriker E. C., 2012, ApJ, 754, 2
Shimajiri Y., et al., 2015, ApJS, 217, 7
Solomon P. M., Vanden Bout P. A., 2005, ARA&A, 43, 677
Solomon P. M., Rivolo A. R., Barrett J., Yahil A., 1987, ApJ, 319, 730
Sun J., et al., 2018, ApJ, 860, 172
Swinbank A. M., Smail I., Sobral D., Theuns T., Best P. N., Geach J. E., 2012, ApJ, 760, 130
Tacconi L. J., et al., 2013, ApJ, 768, 74
Tacconi L. J., et al., 2018, ApJ, 853, 179
Tamburello V., Mayer L., Shen S., Wadsley J., 2015, MNRAS, 453, 2490
Teyssier R., Chapon D., Bournaud F., 2010, ApJ, 720, L149
Tomczak A. R., et al., 2016, ApJ, 817, 118
Toomre A., 1964, ApJ, 139, 1217
Usero A., et al., 2015, AJ, 150, 115
Utomo D., et al., 2017, ApJ, 849, 26
Vazdekis A., Koleva M., Ricciardelli E., Röck B., Falcón-Barroso J., 2016, MNRAS, 463, 3409
Virtanen P., et al., 2020, Nature Methods, 17, 261
Wei L. H., Keto E., Ho L. C., 2012, ApJ, 750, 136
Weiner B. J., et al., 2006, ApJ, 653, 1027
Whitaker K. E., van Dokkum P. G., Brammer G., Franx M., 2012, ApJ, 754, L29
Whitaker K. E., et al., 2014, ApJ, 795, 104
White H. A., et al., 2017, ApJ, 846, 35
Wiklind T., et al., 2019, The Astrophysical Journal, 878, 83
Williams J. P., de Geus E. J., Blitz L., 1994, ApJ, 428, 693
Wisnioski E., Glazebrook K., Blake C., Poole G. B., Green A. W., Wyder T., Martin C., 2012, MNRAS, 422, 3339
Wisnioski E., et al., 2015, ApJ, 799, 209
Wuyts S., et al., 2011, ApJ, 742, 96
de Blok W. J. G., Walter F., Brinks E., Trachternach C., Oh S. H., Kennicutt R. C. J., 2008, AJ, 136, 2648
den Brok J., Chatzigiannakis D., Bigiel F., Puschnig J., 2021, MNRAS
van der Kruit P. C., 1988, A&A, 192, 117

## APPENDIX A: OBSERVED VS. MODELED MOMENT MAPS

This paper has been typeset from a TEX/LATEX file prepared by the author.

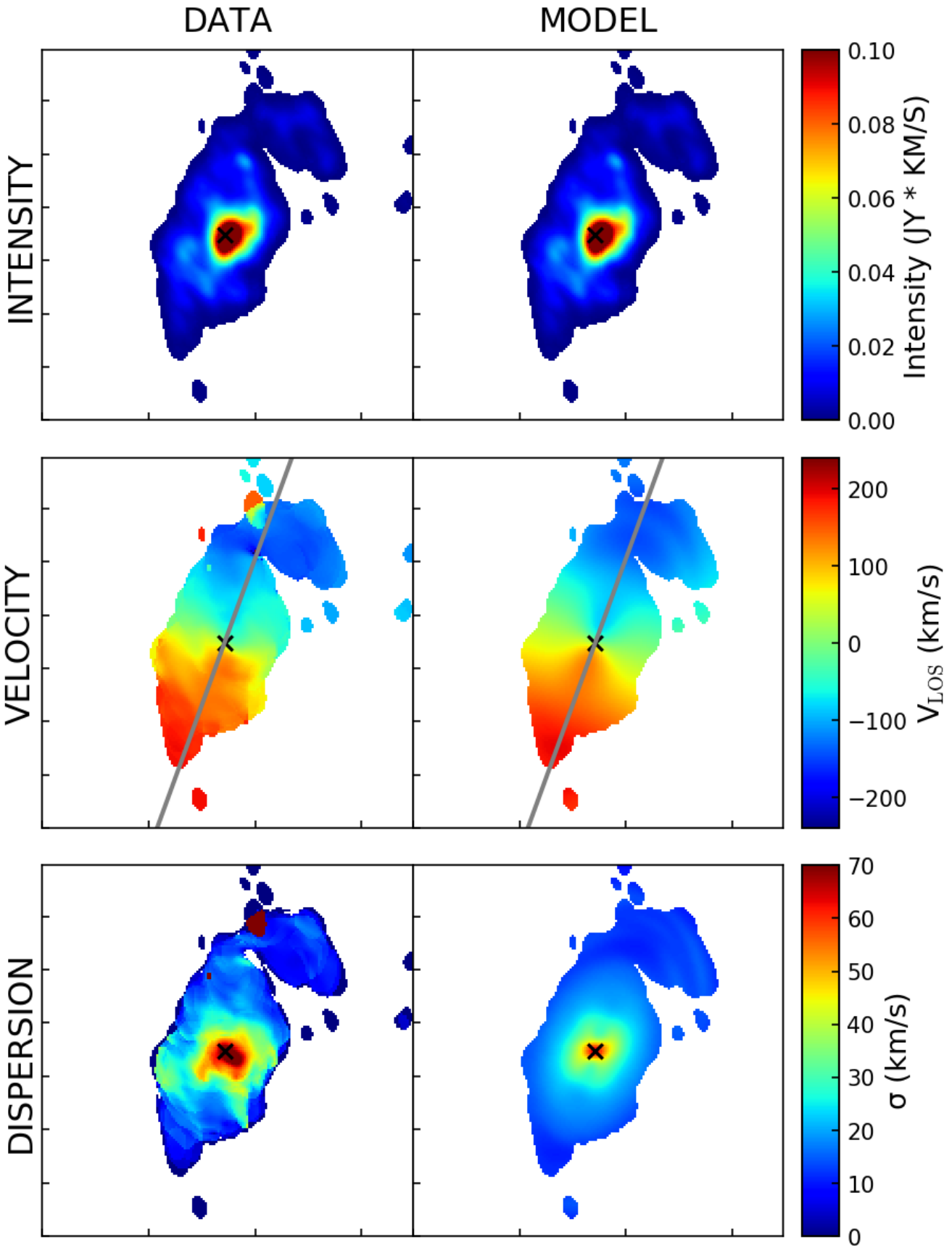



**Figure A1.** Observed (*left column*) versus modeled (*right column*) properties of LARS 8. The latter were produced with $^{3D}$BAROLO.